RSC Advances

PAPER

View Article Online
View Journal | View Issue

Cite this: *RSC Adv.*, 2025, **15**, 32638

Molecular energy transfer: utilizing biogenically-synthesized $ZnMn_2O_4$ nanoparticles from *Arachis hypogaea* seeds for photoluminescence, adsorption, and photocatalytic applications

Aakash Venkatesan, [a] Aatika Nizam, *[a] Anila Rose Cherian, [a] Rupali Patel, [b] Jobi Xavier, [c] Pooja K R,[d] Harini R[e] and Nagaraju G *[f]

The green synthesis of nanoparticles (NPs) has emerged as a sustainable alternative to conventional chemical approaches, primarily due to the use of phytochemicals as reducing and stabilizing agents. In the present study, bimetallic $ZnMn_2O_4$ nanoparticles were synthesized *via* a green combustion method employing *Arachis hypogaea* (peanut) seed powder as a natural fuel source. The synthesized $ZnMn_2O_4$ NPs were systematically characterized using XRD, FTIR, SEM, BET, UV-Vis, and PL spectroscopy to elucidate their structural, morphological, and optical properties. Distinct bluish-green fluorescence was observed under short-wave UV irradiation (254 nm), enabling their application in latent fingerprint visualization. The multifunctional performance of the $ZnMn_2O_4$ NPs was further demonstrated in environmental applications. The materials exhibited enhanced adsorption (63% ± 0.2%) and photocatalytic degradation (79% ± 0.3%) efficiencies against Methylene Blue (MB) dye under UV irradiation, with results statistically significant ($p < 0.05$). In addition, the NPs effectively reduced toxic Cr(VI) ions in aqueous media, highlighting their potential as efficient detoxification agents. Overall, this work demonstrates a novel, green synthesis route for $ZnMn_2O_4$ nanoparticles that uniquely integrates environmental remediation and forensic applications. The dual functionality addressing both pollutant degradation/detoxification and forensic fingerprint visualization positions this study as a rare and innovative contribution to the field of nanotechnology.

Received 5th August 2025
Accepted 25th August 2025

DOI: 10.1039/d5ra05696a

rsc.li/rsc-advances

1. Introduction

In the past two decades, the advancement of nanotechnology has been tremendous. It can be attributed to the unique physical and chemical properties[1] of nanomaterials that led them to be utilized in a diverse range of scientific fields, including chemistry,[2] biology,[3] physics,[4] engineering,[5] materials science[6] and medicine.[7] The distinctive properties of nano materials are their nano range with a large surface area as compared to the micro range of similar materials. Thus, intensive research has been undertaken by researchers to expand the usage of Nanomaterials in multidisciplinary fields such as medical therapeutics,[8] structural materials,[9] energy production[10] and degradation of organic effluents.[11] Upon investigation of the multidisciplinary aspects, a class of nanotechnology known as semiconductor nanoparticles has drawn the attention of researchers due to spatial quantum confinement[12] and tunable alteration in the band gap, which can contribute chiefly in various applications.[13]

The transition metal oxides possess both semiconductor properties and excellent redox properties due to their empty d orbitals, which readily lose or capture electrons, making them an ideal metal oxide catalyst.[14] Among these semiconductor transition metal oxide nanoparticles, Zinc oxide (ZnO) is extensively used in a variety of industries, including the production of UV light-emitting diodes and lasers[15] due to its sensitive reactivity towards both visible and ultraviolet light.[16] Furthermore, ZnO is frequently employed as a heterogeneous catalyst in the chemical industry to produce a wide range of compounds, including methanol.[17] However, ZnO's limited reusability, rapid electron–hole recombination, and poor adsorption ability limit its catalytic efficacy.[18] Additionally, oxides of manganese are known to play significant catalytic roles in various organic reactions due to their high redox and catalytic properties.[19] The spinel structure of AB_2O_4 is more

[a]*Department of Chemistry, Christ University, Bangalore-560029, India. E-mail: aatika.nizam@christuniversity.in*

[b]*Department of Physics, Christ University, Bangalore-560029, India*

[c]*Department of Life Sciences, Christ University, Bangalore-560029, India*

[d]*Department of Chemistry, Rani Channamma University, Belagavi 591156, India*

[e]*Department of Electronics and Communication Engineering, Govt. Polytechnic, Hiriyuru – 577599, India*

[f]*Energy Materials Research Laboratory, Department of Chemistry, Siddaganga Institute of Technology, Tumakuru 572103, India. E-mail: nagarajugn@gmail.com*

appealing than conventional single-metal oxides because they may electron-hop between the various valence states of the metals at O-sites and provide the surface active metal centers that are required for redox reactions.[20] Various researchers have synthesized different metal oxides such as $MnFe_2O_4$,[21] $Nd_2Sn_2O_7$,[22] $CuMn_2O_4$.[23],[24] Among these, zinc manganate ($ZnMn_2O_4$) has garnered significant interest owing to its novel characteristics and extensive usage in various fields including magnetic resonance imaging, lithium ion batteries, catalysis, solid electrolytes, and photocatalysis.[25] It is also used in the forensic department to identify the secondary and tertiary information in the fingerprints. This can be attributed to the highly fluorescent emissive nature of the NPs when an excited electron degenerates to the ground state.[26] One of the major drawbacks researchers were facing in the early 20th century was the sustainable synthesis of these semiconductor nanomaterials without the use of toxic chemicals. The chemical method includes sol–gel,[27] hydrothermal,[28] and electrochemical synthesis,[29] which release toxic compounds. Therefore, a sustainable approach has been employed in using biological extracts as the precursors for bio-reduction and stabilization of the nanoparticles.[30] This accounts for the eco-friendly synthesis due to the utilization of phytochemicals such as phenolic compounds, vitamins, polysaccharides, proteins, flavonoids, organic acids, and steroids present in the bio-extracts for the formation and increasing the stability of nanoparticles.[31] Additionally, seeds are rich sources of polysaccharides due to their storage function, and peanuts in particular contain additional natural oils. These components generate an exothermic environment during combustion and release large volumes of gases (CO_2, H_2O, N_2), which facilitate the formation of porous nanoparticles with higher surface area and reduced crystalline size.[30]

Rapid industrialization has brought a low concentration of pollutants with higher levels of toxicity in the aquatic environment.[32] Recalcitrant organic compounds such as pesticides, dyes, hormones, pharmaceuticals, and surfactants from various sectors of the industry are seen as a major threat to water contamination.[33] These organic pollutants, when released into water bodies, undergo anaerobic degradation to form carcinogenic amines, which are toxic to the aquatic organisms and the environment.[34] This also causes human disorders, which include nausea, skin ulcerations, and hemorrhage.[35] Therefore, the necessity to treat the toxic organic pollutants has become important in the current scenario. Various strategies, such as adsorption,[36] coagulation/flocculation,[37] biodegradation,[38] advanced oxidative degradation[39] and photocatalysis[40] have been employed for the treatment of organic pollutants. Among these photocatalytic properties of transition metal oxides, along with semiconducting, catalytic, and redox properties, prevailed in their territory in the degradation of various organic pollutants.[41] Therefore, in this study, we have synthesized a bimetallic transition metal oxide, zinc manganate ($ZnMn_2O_4$), employing a traditional green combustion method with peanut powder as the fuel, which contains a rich source of sucrose and natural oils. Characterizations such as XRD, FTIR, UV-Vis, SEM, and BET were performed to determine the surface morphological characteristics of the synthesized $ZnMn_2O_4$ nanoparticles. Catalytic properties of $ZnMn_2O_4$ nanoparticles were evaluated by subjecting the NPs to the photodegradation of methylene blue dye and detoxification of chromium ions. Photostability was also examined for the commercialization of the NPs in industrial usage for the degradation of organic pollutants.

2. Experimental procedure

2.1. Materials used

The Analytical grade chemicals, such as manganese nitrate [$Mn(NO_3)_2 \cdot 4H_2O$], zinc nitrate [$Zn(NO_3)_2 \cdot 6H_2O$], methylene blue dye, and potassium dichromate ($K_2Cr_2O_7$), purchased from Merck, were used without further purification. Raw peanuts were obtained from a local market in Tumakuru, Karnataka, India.

2.2. Synthesis of $ZnMn_2O_4$ nanoparticles

Based on previously reported methods,[42] the $ZnMn_2O_4$NPs were synthesized by the combustion method using peanut powder as fuel. The raw peanuts were initially ground into a fine powder using a blender. A 1 : 1 stoichiometric molar ratio of 0.1 M Manganese nitrate and 0.1 M Zinc nitrate was dissolved in 10 mL of deionized water along with half the amount of peanut powder. The solution was continuously stirred until it became a homogeneous suspension. Then, the solution was kept in the muffle furnace at 500 °C for about 10 min. After that, a brownish-black foam-like product is formed. The above experiment was repeated for different amounts (double and triple) of fuel with the same molar ratio of precursors. The brownish-black foam obtained was ground into fine powder and calcinated in a muffle furnace at 600 °C for 3 h, with a heating rate of 5 °C min^{-1}. Then, calcinated NPs were used for further characterization and application purposes.

2.3. Characterisation and instrumentations

The crystal structure and the size of $ZnMn_2O_4$ NPs were analysed using a Rigaku Martlab X-ray diffractometer (XRD) with monochromatized CuKα radiation (1.5418 Å) in a 2θ range of 10–70. Functional group and M–O bond of molybdate were analysed using FTIR (Bruker Alpha P-spectrophotometer) in the wavenumber range 350 to 4000 cm^{-1}. The optical properties of the NPs were evaluated using an Agilent Technology Cary-60 UV-Vis diffuse reflectance spectrophotometer (UV-Vis DRS) in the range of 200 to 800 nm. The specific surface area of the catalysts was determined through N_2 adsorption–desorption isotherms using the BET method (BELSORP MINI X). The catalyst was degassed at 120 °C to remove undesired gases from the surface. The photoluminescence spectrum of $ZnMn_2O_4$ nanoparticles was measured using an Agilent Technology Cary Eclipse fluorescence spectrophotometer at an excitation wavelength of 222 nm. The photo degradation of dyes was analysed in an Agilent Technology Cary-60 UV-Vis absorption spectrophotometer.

2.4 Adsorption studies

The adsorption of methylene blue dye was examined by introducing a certain amount of absorbent ($ZnMn_2O_4$NPs) to 20 mL of MB dye solution at room temperature. The parameters optimized for efficient adsorption are contact time and dye concentration, where the conditions of the optimization for these parameters are provided in the SI. The effects of dye concentration on adsorption were examined at different ppm levels (25–100 ppm), and the effect of time was evaluated by varying time intervals (0–18 min). The percentage adsorption of MB dye by $ZnMn_2O_4$ NPs was examined using a UV-Vis absorption spectrophotometer by observing the absorbance of the MB dye solution at λ_{max} of 665 nm. The adsorption percentage was calculated by the equation below.[43]

$$\% \text{ of adsorption} = [A_0 - A_t/A_0] \times 100 \quad (1)$$

where, A_0 is the initial concentration of the MB dye solution and A_t is the concentration of the MB dye solution.

2.5 Photocatalytic degradation studies

The photo-catalytic activity of $ZnMn_2O_4$ NPs was evaluated by methylene blue (MB) degradation under a UV-light source. To assess the photo-catalytic activity, 5–20 mg of $ZnMn_2O_4$ NPs were weighed and uniformly distributed in the dye solution (5–20 ppm). Then the solution was placed in the dark for 30 min to attain the adsorption–desorption equilibrium between NPs and the dye solution. Once the equilibrium was achieved, the homogenous solution was exposed to UV light radiation in a Herber UV-visible photoreactor. At an interval of 30 minutes, the dye solution was withdrawn from the reactor until the solution became colorless and centrifuged to settle or separate the nanoparticles. The percentage degradation of MB dye by $ZnMn_2O_4$ NPs was examined using a UV-Vis absorption spectrophotometer by observing the absorbance of the MB dye solution at λ_{max} of 665 nm. The percentage degradation was calculated by the equation below.

$$\% \text{ of degradation} = [C_0 - C_t/C_0] \times 100 \quad (2)$$

where, C_0 is the initial concentration of the MB dye solution, and C_t is the concentration of the MB dye solution collected at an interval of 30 minutes.[19]

2.6 Photocatalytic detoxification studies

The photocatalytic detoxification of chromium(IV) ions was performed by adding 5 mg of $ZnMn_2O_4$ NPs to 100 mL (1 mM) $K_2Cr_2O_7$ solution, irradiated under a UV light source at neutral pH. A known volume (2 mL) of the irradiated solution was withdrawn at a time interval of 30 min until it became colourless. Then, the withdrawn solution was centrifuged to separate the nanoparticles. The percentage reduction of Cr(IV) to Cr(III) ions by $ZnMn_2O_4$ NPs was examined using a UV-Vis absorption spectrophotometer by observing the absorbance of $K_2Cr_2O_7$ solution at 350 nm. The percentage degradation was calculated by the equation below.

$$\% \text{ of reduction} = [A_0 - A_t/A_0] \times 100 \quad (3)$$

where, A_0 is the initial concentration of the $K_2Cr_2O_7$ solution and A_t is the concentration of the $K_2Cr_2O_7$ solution withdrawn at an interval of 30 min.[44]

2.7. Statistical analysis

All experiments were conducted in triplicate to minimize handling errors and ensure reproducibility. Statistical analysis was performed using IBM SPSS Statistics v26 (2019) software with one-way ANOVA, and the results are presented as mean ± standard deviation (SD).

3. Results and discussions

3.1. Powder X-ray diffraction (XRD) pattern analysis

The tetragonal shape of all $ZnMn_2O_4$ NPs with varying fuel concentration formed through the green combustion method was confirmed by X-ray diffractometer. The synthesized $ZnMn_2O_4$ NPs XRD patterns are depicted in Fig. 1a. For all $ZnMn_2O_4$ (1 : 0.5, 1 : 1, 1 : 1.5) the peaks at 2θ = 18.22, 29.32, 31.23, 33.01, 36.40, 38.97, 44.76, 51.97, 54.41, 56.73, 59.00, 60.82, 65.16 which are indexed to the planes (101), (112), (200), (103), (211), (004), (220), (105), (312), (303), (321), (224), (400) respectively. The peaks are matching with JCPDS card no: 71-2499.[14] It was observed that on increasing the fuel concentration the intense XRD peak at 2θ = 36.40 which is noted in all samples with the planes (211) preferred the growth but in fuel rich concentration of $ZnMn_2O_4$ (1 : 1.5) NPs the intense XRD peak at 2θ = 29.32, 31.23, 33.01, 36.40 with plane (112), (200), (103), (211) showed bifurcations through which peak shift was observed which resulted in the broadening of the peaks. This can be attributed to the increased micro-strain as well as the decreased crystalline size in fuel-rich concentration of $ZnMn_2O_4$ (1 : 1.5) NPs.[45]

The average crystal sizes of the synthesized $ZnMn_2O_4$ NPs were calculated using Debye–Scherrer's equation.[46]

$$D = \frac{K\lambda}{\beta \cos \theta} \quad (4)$$

where, D is the crystallite size, λ is the wavelength of the X-ray (1.54 Å) used, β is the full-width at half maximum (FWHM), and θ is the diffraction angle. Additionally, the lattice parameter of the $ZnMn_2O_4$ NPs was calculated for the prominent peak at 2θ = 36.40 (211) using Bragg's equation:[46]

$$a = d(h^2 + k^2 + l^2) \quad (5)$$

where a represents the lattice parameter, d is the distance between parallel lattice planes with Miller indices (hkl). The micro-strain of the sample was calculated using the equation given below.[45]

$$\varepsilon = \frac{\beta}{4\tan \theta} \quad (6)$$

where ε represents the micro strain, β is the full-width at half maximum (FWHM), and θ is the diffraction angle. The

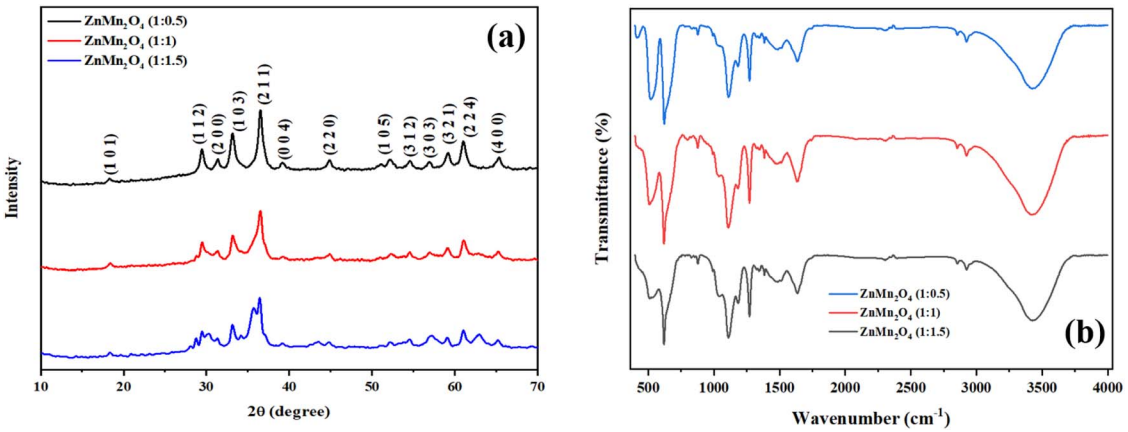

Fig. 1 (a) XRD pattern of $ZnMn_2O_4$ NPs synthesized at different ratios (b) FTIR spectrum of $ZnMn_2O_4$ NPs prepared at different ratios.

Table 1 The crystalline size and lattice parameters of $ZnMn_2O_4$ NPs

Type of nanoparticle	Crystalline size (nm)	Lattice parameter (Å)	Microstrain ($\times 10^{-3}$)
$ZnMn_2O_4$ (1 : 0.5)	13.05	6.0405	8.41
$ZnMn_2O_4$ (1 : 1)	12.56	6.0405	9.24
$ZnMn_2O_4$ (1 : 1.5)	11.49	6.8788	9.59

crystalline size, lattice parameter, and strain of the synthesized nanoparticles are compiled in Table 1.

3.2. Fourier transform infrared spectroscopy (FTIR) analysis

Fig. 1b and S1, SI, shows the FTIR spectra of $ZnMn_2O_4$ NPs between the ranges 350–4000 cm^{-1}. The highest frequency peak corresponding to 619 cm^{-1} is attributed to the stretching mode of Mn–O at the tetrahedral site, and the peak corresponding to 510 cm^{-1} is attributed to the stretching mode of Zn–O at the hexagonal phase[47] where the absorption band of Zn–O ranges from 800 to 400 cm^{-1}.[48] The peak attributed to the stretching mode of Zn–O was reduced, and the high-frequency peak of Mn–O became narrower as the concentration of fuel increased, as shown in Table S1. The narrow peaks at 1109 cm^{-1} and 1270 cm^{-1} are owed to the C–O stretching bond and C=C vibration bond, whereas the broad peaks at 1484 cm^{-1} and 3423 cm^{-1} are ascribed to the C–H bending and O–H functional group. The peak shouldered at 1635 cm^{-1} contributes to the C=O stretching vibration modes. This indicates that the polysaccharides and natural oils, which are abundantly present in the peanut seeds, act as capping agents on the surface of $ZnMn_2O_4$ nanoparticles.

3.3. UV-visible spectroscopy studies

The optical properties and energy band gap of $ZnMn_2O_4$ NPs were evaluated using UV-Vis DRS spectroscopy. The spectral data divulged that absorption edges lie in the 200 to 600 nm of the visible region and shift towards the lower wavelength (blue shift) on increasing the fuel concentration.

The optical band gap energy of synthesized NPs was obtained by analysing the reflectance spectra represented in Fig. 2a using the Kubelka–Munk relation, which is used to convert the reflectance to the Kubelka–Munk function $F(R)$.[49]

$$F(R) = \frac{(1-R)^2}{2R} \tag{7}$$

where R is the reflectance value. The photon energy corresponding to the wavelength can be evaluated using the following relation.

$$E_g = \frac{hc}{\lambda}\text{eV};\quad E_g = \frac{1240}{\lambda}\text{eV} \tag{8}$$

where E_g is the band gap energy (eV), h is Planck's constant (6.626×10^{-34} J s), c is the light velocity (3×10^8 m s^{-1}), and λ is the wavelength (nm). The optical band gap of the NPs was estimated by plotting a graph and varying the Kubelka–Munk function along with photon energy, which is presented in Fig. 2b. It reveals that on increasing the fuel concentration, the band gap of the NPs varies. The crystalline size of the semiconductor NPs has a huge impact on its band gap. Due to the smaller crystalline size of the $ZnMn_2O_4$ with a fuel concentration ratio of 1 : 1.5, the NPs are subjected to the quantum confinement effect, leading to a higher band gap.[50] Thus, $ZnMn_2O_4$ with a fuel concentration ratio of 1 : 1 shows the lower band gap energy of 4.10 eV, which can exhibit enhanced performance in photo-catalytic degradation of dye by the generation of more electron/hole pairs under UV light irradiation. The energy band gap is directly correlated with the energy needed to drive an electron from the valence band to the conduction band.[51] The position of the valence band and the conduction band has a significant influence on the photocatalytic mechanism.[52] Thus, by using the Mulliken electronegativity relation, the position of the valence band and the conduction band are estimated.[53]

$$E_{vb} = \chi - E^0 + 0.5E_g \tag{9}$$

$$E_{cb} = \chi - E^0 + 0.5E_g \tag{10}$$

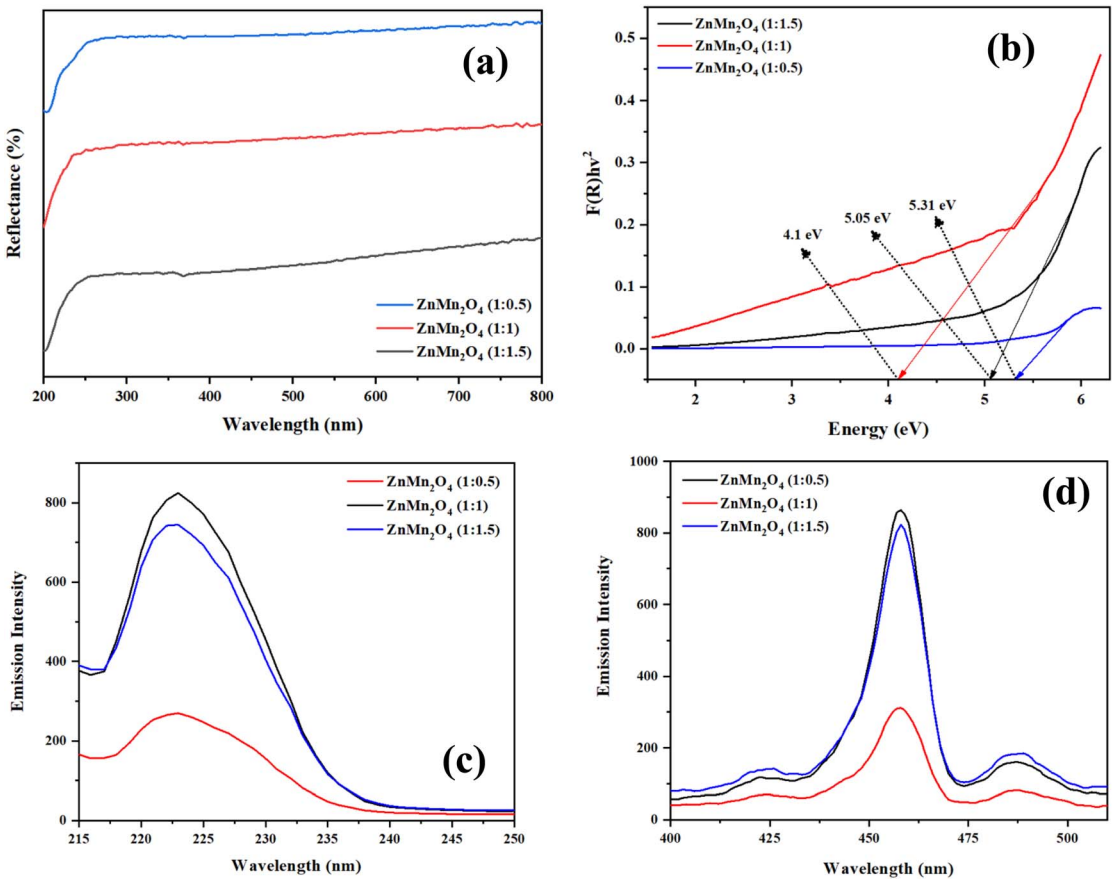

Fig. 2 (a) UV-visible spectrum of $ZnMn_2O_4$NPs (1 : 0.5, 1 : 1, 1 : 1.5) (b) Kubelka–Munk plot (c) excitation spectrum ($\lambda_{emission} = 456$ nm) (d) emission spectrum ($\lambda_{excitation} = 222$ nm).

where χ, the absolute electronegativity of $ZnMn_2O_4$, was found to be 5.78, calculated using the formula.[54]

$$\chi = [x(A)^a x(B)^b x(C)^c]^{1/a+b+c} \quad (11)$$

E^0 is the constant value of free electron energy on the hydrogen scale (4.5)[53] and E_g is the optical band gap of the material. The obtained bandgap, valence band, and conduction band of the NPs are summarised in Table S2, SI.

3.4. Photoluminescence (PL) analysis

PL spectra were recorded by measuring the emission of light released when the photo-generated electron/hole recombines. This spectrum was used to evaluate the basic radiative properties of the synthesized $ZnMn_2O_4$ NPs and the charge separation efficiency. Fig. 2c and d show the photoluminescence emission and excitation spectra of all synthesized $ZnMn_2O_4$ NPs. The excitation wavelength of the sample is found to be 222 nm, whereas the emission peaks are shouldered at 456 nm and 487 nm. The main emission peak shouldered at 456 nm, which is due to oxygen vacancies. Among the synthesized NPs$ZnMn_2O_4$ (1 : 1), NPs showed a lower emission intensity, which can be attributed to the greater charge separation.[55] This property of $ZnMn_2O_4$(1 : 1) NPs can facilitate a higher photodegradation percentage than the other synthesized NPs.

The CIE 1931 *x*-*y* chromaticity diagram (Commission Internationale de l'Elcairage) is plotted for the colour detection of light emitted by NPs, represented in Fig. S2, SI. The purity of colour can be observed with the chromaticity points. The respective chromaticity points for the synthesized $ZnMn_2O_4$ (1 : 0.5, 1 : 1, 1 : 1.5) NPs are (0.287, 0.287), (0.218, 0.234), (0.197, 0.19). The different *x* and *y* coordinates demonstrate the ionic liquid's significant influence on the crystallization process as well as the high hue and purity of the light emitted.

3.5. Scanning electron microscope (SEM) and energy-dispersive X-ray (EDX) analysis

The SEM images of synthesized $ZnMn_2O_4$ (1 : 1) NPs at different magnifications are shown in Fig. 3a–d. The nano range of the NPs is observed, and on changing the magnification to 300 nm, which is depicted in Fig. 3c, two distinct morphologies of $ZnMn_2O_4$ (1 : 1) NPs were observed, which are similar to wheat[56] and fiber-type structures.[57] The agglomeration of the NPs is also observed, which can be attributed to the high surface area energy, which causes the NPs to form bundles, and as the temperature of the NPs reduces to room temperature after the growth, the enthalpy becomes negative. Therefore, to maintain the equilibrium, the NPs' size changes and agglomerate.[56] The EDX spectra of the synthesized NPs are shown in Fig. 6e. It reveals that the sample contains Zn, Mn, and O with a definite

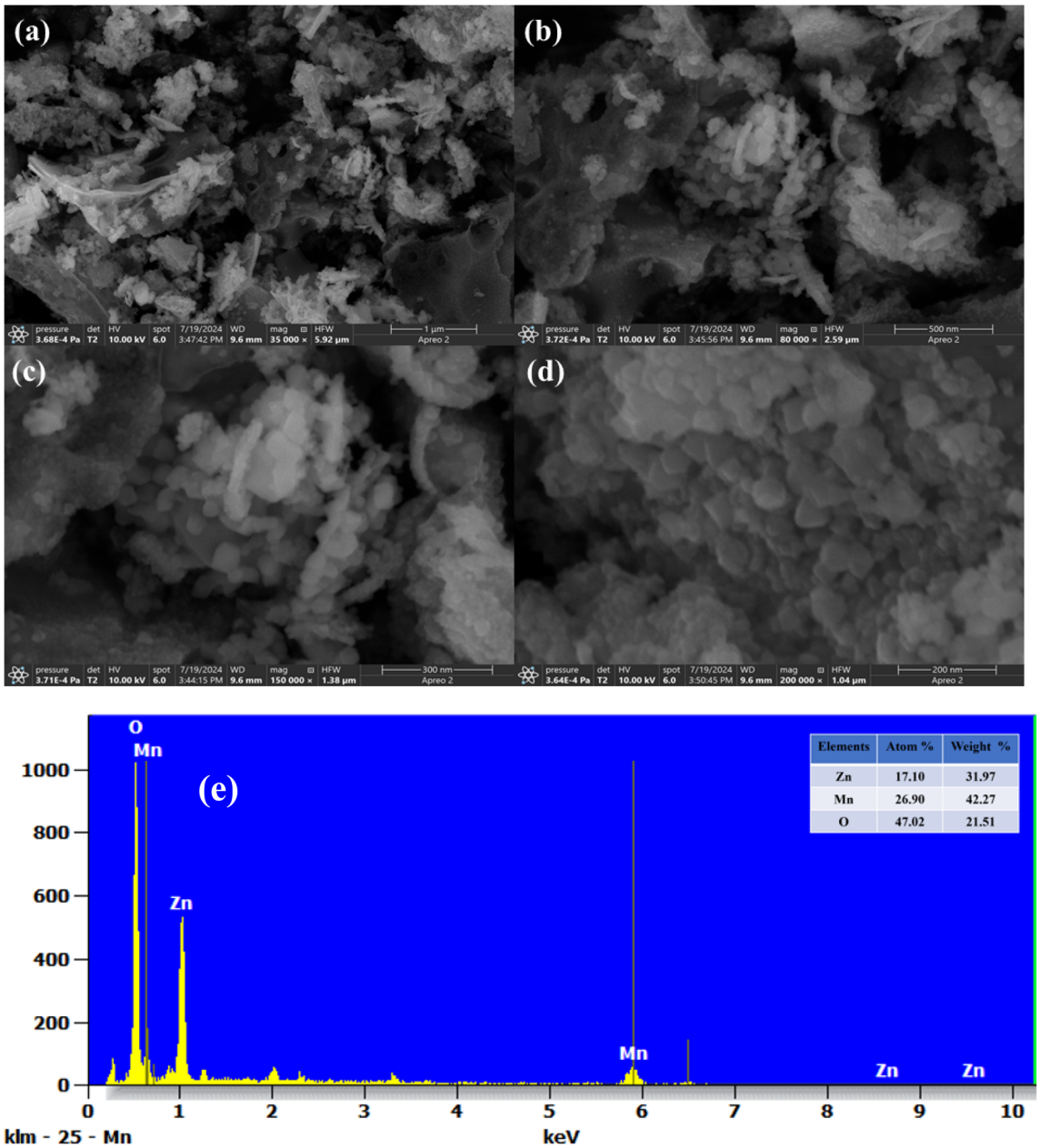

Fig. 3 (a–d) SEM micrographs and (e) EDX pattern of $ZnMn_2O_4$ NPs prepared at 1 : 1 ratio.

stoichiometry expected (Zn : Mn: O = 1 : 2:4). The values of weight% and atom% of $ZnMn_2O_4$ (1 : 1) NPs were recorded using EDX measurements.

3.6. Brunauer–Emmett–Teller (BET) analysis

Fig. 4a shows the nitrogen adsorption–desorption isotherm of $ZnMn_2O_4$ powder. A typical type III isotherm with a minor hysteresis loop is detected, which suggests the presence of interconnected macropores formed due to the random arrangement of $ZnMn_2O_4$ NPs. The specific area is determined as 30 m^2 g^{-1} with a pore diameter of 10 nm and pore volume of 0.1517 cm^3 g^{-1} formed within the porous network as depicted from the pore size distribution curve in Fig. 4b. This pore structure facilitates the fast diffusion of foreign ions, thereby increasing the number of active sites available. $ZnMn_2O_4$ nanostructures synthesized *via* other methods typically exhibit surface areas in the range of 15–35 m^2 g^{-1}, depending on synthesis conditions and morphology. Thus, the BET surface area of 30 m^2 g^{-1} obtained in our study is comparable to, or slightly higher than, many conventionally synthesized counterparts, which can be attributed to the unique combustion environment created by the use of peanut seed powder as a green fuel.

3.7. Transmission electron microscopy (TEM) analysis

The transmission electron microscopy (TEM) image reveals the nanorods of $ZnMn_2O_4$ NPs, and the moderate aggregation seen

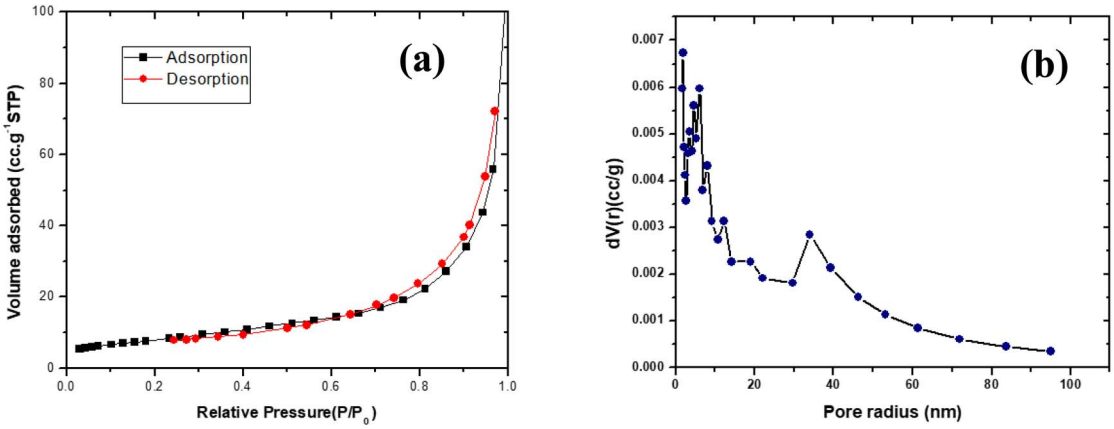

Fig. 4 (a) Nitrogen adsorption–desorption isotherm of $ZnMn_2O_4$ NPs, (b) pore size distribution curve of $ZnMn_2O_4$ NPs.

in the scanning electron microscope (SEM) may originate from the NPs high specific surface energy. The transmission electron microscopy (TEM) images displayed in Fig. 5–c revealed the nanorods of the particles, which have an average size of 20 nm. The $ZnMn_2O_4$ NPs HR-TEM is shown in Fig. 5d. The difference between the two successive plans is $d_{211} = 0.52$ nm.

3.8. Adsorption property

3.8.1. Contact time. Fig. 6a represents the effect of contact time in the adsorption of MB dye (50 ppm) at varying time intervals (18 min) by 5 mg of $ZnMn_2O_4$ NPs. The adsorption percentage plot of MB dye at various contact durations is given

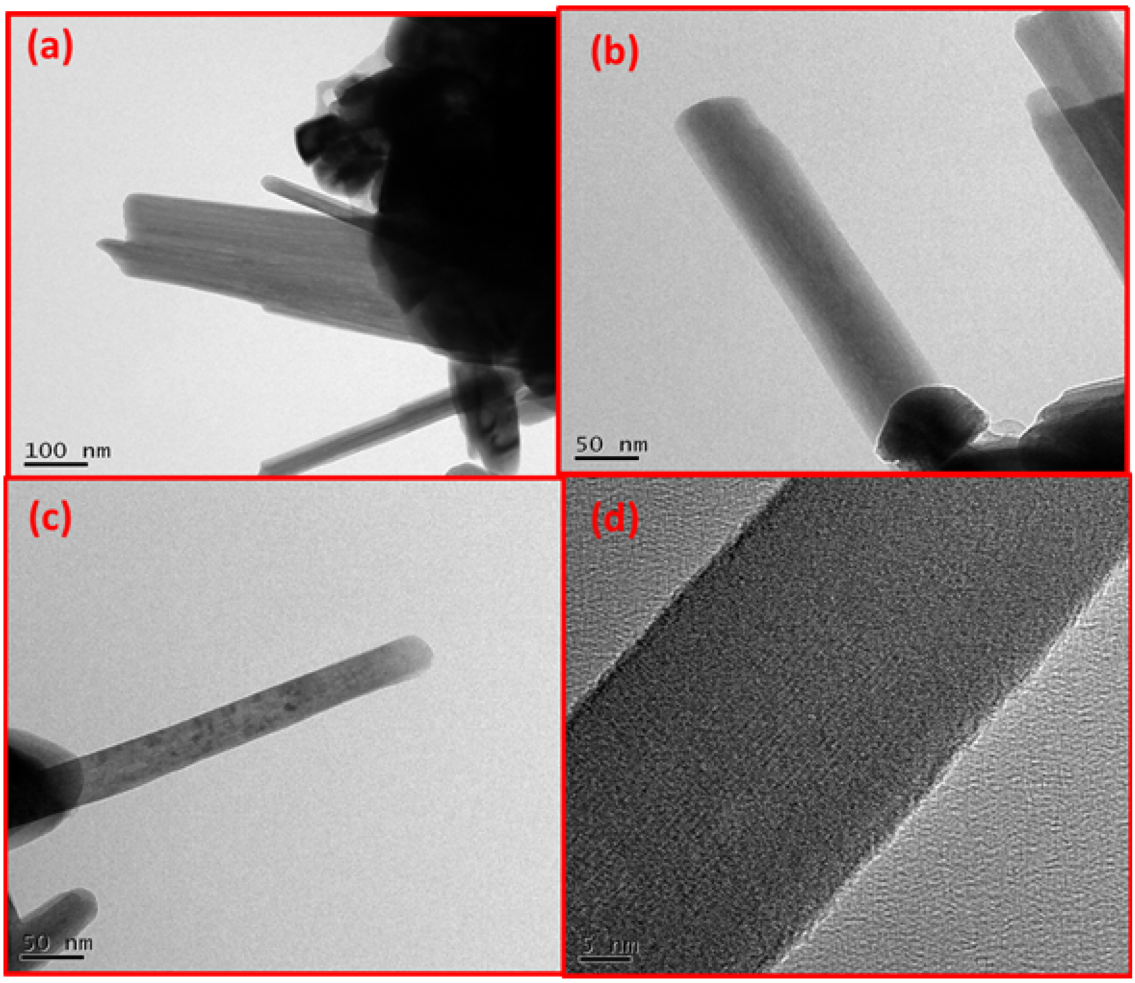

Fig. 5 (a–c) TEM images and (d) HR-TEM image of $ZnMn_2O_4$NPs, approximately $d = 0.26$ nm, corresponding to the (311) plane.

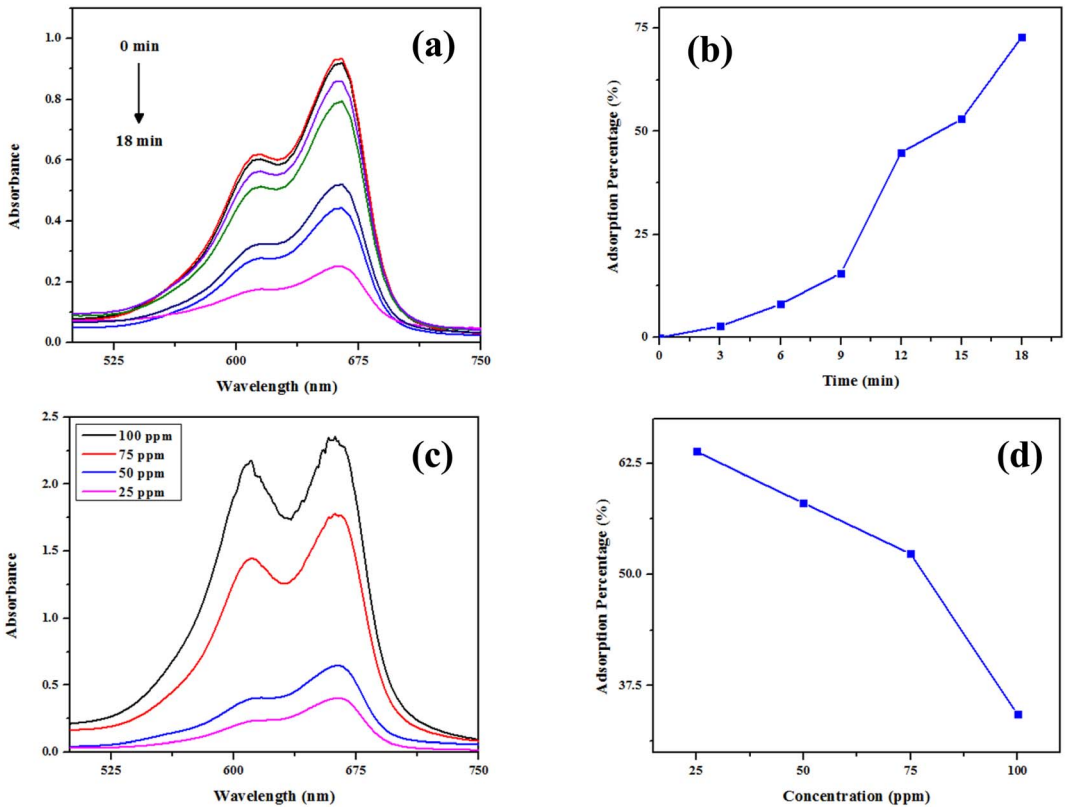

Fig. 6 (a) Adsorption of MB dye at varying time durations (0–18 min) (b) adsorption percentage of MB dye with respective to time. (c) UV spectra of adsorption of MB in varying concentrations of dye (d) adsorption percentage of MB in varying concentrations of dye.

in Fig. 6b. It is observed that as time increases, the adsorption rate also increases and reaches a saturation point. Maximum adsorption was observed at 18 min. This can be attributed to the availability of more active sites for the adsorption initially. As the process proceeds, there is a reduction in the availability of the active sites, which are occupied by the dye molecules.[58] A phase time (18 min), in which the availability of the active site vanishes and a saturation point is obtained, and further adsorption is inhibited. Thus, 18 min is the optimum time for the maximum adsorption of MB dye by $ZnMn_2O_4$ NPs.

3.8.2. Dye concentration. Adsorption of MB at varying dye concentration was evaluated and represented in Fig. 6c. Different dye concentrations of 25 ppm, 50 ppm, 75 ppm, and 100 ppm were utilized along with 5 mg of $ZnMn_2O_4$ NPs to perform this experiment. It is noted that the adsorption percentage decreased on increasing the concentration of MB dye, and maximum adsorption took place in 25 ppm solution. This behavior of absorbent can be ascribed to the reduction in the surface area and binding sites as the concentration of dye increases.[59] In case of low dye concentration, the number of available binding sites is larger compared to the amount of MB dye molecules. As a result, the absorption percentage is higher at lower dye concentrations, as given in Fig. 6d. Conversely, on increasing dye concentration, only a few binding sites are available for the dye molecules to bind, which creates a competition between the molecules and reduces the adsorption percentage. Once the monolayer of absorbent is covered by the dye molecules, there are no more binding sites for the dye molecules to adsorb, and further adsorption is hindered.

3.8.3. Adsorption Kinetics. Two kinetic models are used to evaluate the impact of contact time on the adsorption of MB dye by $ZnMn_2O_4$: the pseudo-first-order model demonstrated by Lagergren[60] and the pseudo-second-order equation propounded by Ho and McKay.[61] The equation below, which is a pseudo-first-order kinetic equation, is a basic kinetic model intended to clarify the adsorption mechanism in solid/liquid systems. On the other hand, the adsorption equilibrium capacity is the basis of the pseudo-second-order equation below.

$$\log(q_e - q_t) = \log q_e - \frac{k_1 t}{2.303} \quad (12)$$

$$\frac{t}{q_t} = \frac{1}{K_2 (q_e)^2} - \frac{t}{q_e} \quad (13)$$

where q_t is the adsorption capacity at time t, k_1 is the pseudo-first-order rate constant (min^{-1}), and k_2 is the pseudo-second-order rate constant (g mg^{-1} min^{-1}). The obtained R^2 value for pseudo-first-order kinetics is 0.84983, whereas for pseudo-second-order kinetics, the R^2 value is 0.96702, illustrated in Fig. 7a and b. Comparatively lower R^2 value of the pseudo-first-order suggests the lowest possible level of interaction between MB dye molecules and a single active site. Additionally, the slightly higher pseudo-second-order R^2 value shows that the dye molecule can interact with two adsorption sites at once. Therefore, a pseudo-second-order reaction describes the

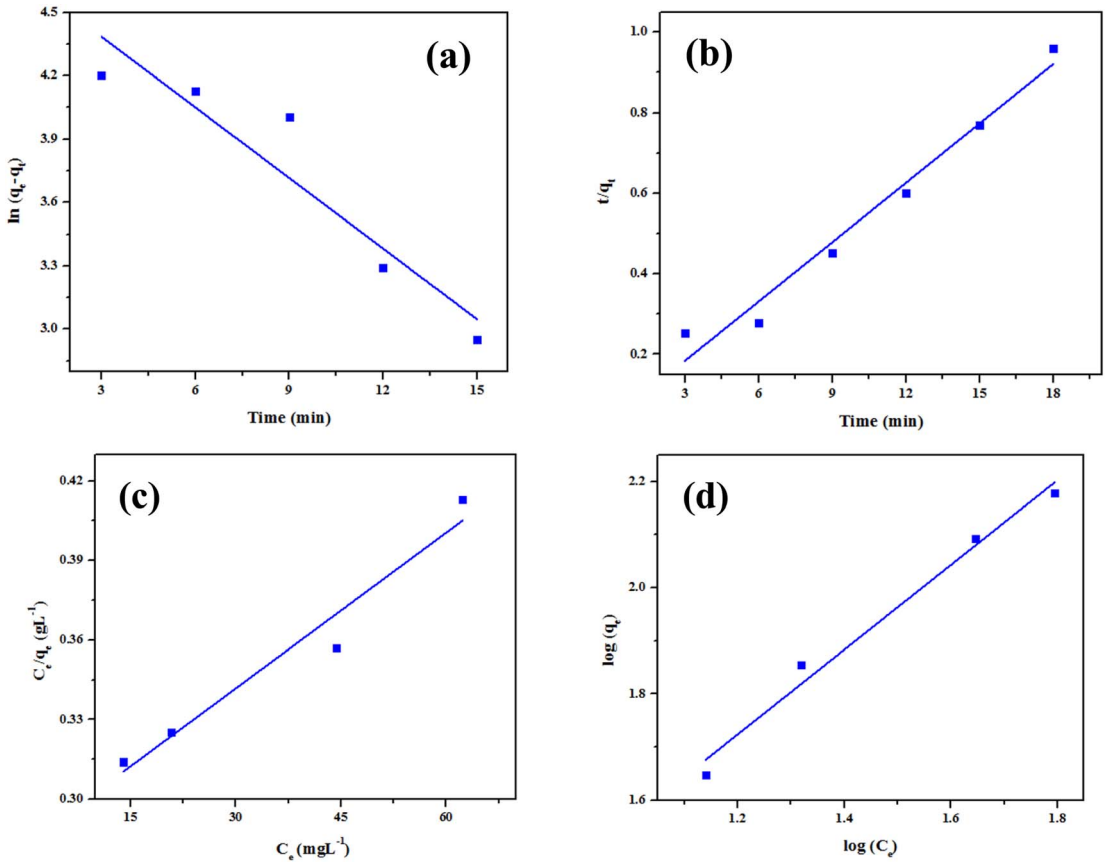

Fig. 7 Adsorption kinetics plots (a) pseudo-first order, (b) pseudo-second order; adsorption isotherm plots (c) Langmuir and (d) Freundlich plot for the adsorption of MB dye.

adsorption of MB dye onto $ZnMn_2O_4$ rather than the pseudo-first-order reaction. This observation also suggests that the dye concentration affects the MB dye's adsorption rate. Table 2 provides the computed values of k_1 and k_2, as well as R^2. The greater value of parameter k from a pseudo-second-order plot quantified the reaction speed.

3.8.4. Adsorption isotherm. The two isotherm equations (Langmuir and Freundlich equations) below can be utilized to explain the adsorption process in general.

$$\frac{C_e}{q_e} = \frac{1}{bq_m} + \frac{C_e}{q_m} \quad (14)$$

$$q_e = K_f C_e^{1/n} \quad (15)$$

where q_m (mg g^{-1}) and b (L mg^{-1}) are Langmuir coefficients. K_f and n are Freundlich constants. The q_m value represents the maximum adsorption capacity, and q_e (mg g^{-1}) is the amount of dye adsorbed at equilibrium, calculated using eqn (16).

$$q_e = \frac{(C_0 - C_e)V}{m} \quad (16)$$

where C_0 (mg L^{-1}) and C_e (mg L^{-1}) are the initial and equilibrium dye concentrations, V (L) is the volume of dye solution, and m (g) is the mass of adsorbent.

According to the Langmuir model, dye molecules are adsorbed as monolayers on the active sites of $ZnMn_2O_4$. Fig. 7c shows the plot C_e/q_e against C_e, which gives the Langmuir coefficients (q_m and b). This coefficient is used to measure the adsorption ability of $ZnMn_2O_4$, where q_m and b are found to be 510 ± 0.5 mg g^{-1} and 0.00692 ± 0.0001 L mg^{-1}. The R^2 value obtained for the Langmuir plot is 0.93855. The lower R^2 value indicates that the monolayer adsorption is hindered. The

Table 2 Kinetic parameters for MB adsorption by $ZnMn_2O_4$ NPs

	Pseudo first order		Pseudo-second order	
Concentration (mg L^{-1})	R^2	k_1 (1 min^{-1})	R^2	k_2 (g mg^{-1} min^{-1})
50	0.84983	0.11139 ± 0.001	0.96702	0.2580 ± 0.002

Table 3 Isotherm parameters for MB adsorption by $ZnMn_2O_4$ NPs

Isotherm	Isotherm parameters	Values
Langmuir	q_m (mg g^{-1})	510.204 ± 0.5
	b (L mg^{-1})	0.00692 ± 0.001
	R^2	0.93855
Freundlich	K_f (mg g^{-1}) (L $mg^{-1})^{1/n}{}_f$	2.154 ± 0.05
	$1/n$	0.79715 ± 0.04
	R^2	0.97591

Freundlich plot is represented in Fig. 7d providing Freundlich constants K_f and n, which describe the heterogeneous sorption phenomenon of adsorption.[43] The K_f and $1/n_f$ values obtained are 2.154 ± 0.05 and 0.79715 ± 0.04. These constants are the essential parameters for determining the extent of favorability of the process. Based on the magnitude of the $1/n_f$, the adsorption process is classified as reversible ($1/n_f = 0$), favorable ($0 < 1/n_f < 1$), and unfavorable ($1/n_f = 1$). The process is favorable in this case, as the magnitude is positive and less than 1. Additionally, n_f can also be used to determine whether the adsorption is physical ($n_f > 1$) or chemical ($n_f < 1$). In this study, the value of n_f is greater than 1. Therefore, it implies the process is favorable physical adsorption. The higher R^2 value (0.97591) confirms that the MB multilayer adsorption occurs on heterogeneous sorption sites with varied adsorption energies.[62] The data is computed in Table 3.

FTIR and SEM analyses were performed to elucidate the morphological changes that occurred after the adsorption of MB dye, as shown in Fig. S3. The FTIR revealed the additional peaks at 1041, 1400, 1625 and 2355 cm^{-1}, which correspond to the bands of MB dye, which coincides with the determined physical adsorption by the Freundlich plot, and the SEM shows high agglomeration, which is due to the adsorption of MB dye onto the surface of $ZnMn_2O_4$ NPs, which neutralizes surface charges. This reduces the electrostatic repulsion between $ZnMn_2O_4$ NPs, allowing them to approach each other and form agglomerates. Therefore, this confirms the adsorption of MB dye onto the $ZnMn_2O_4$ NPs

3.9. Photocatalytic property

3.9.1. Degradation of organic dyes. The photo-catalytic ability of $ZnMn_2O_4$ NPs was evaluated by the degradation of various organic dyes with a constant 5 ppm (pH 7) under a UV light source. Fig. 8a shows the percentage degradation values of

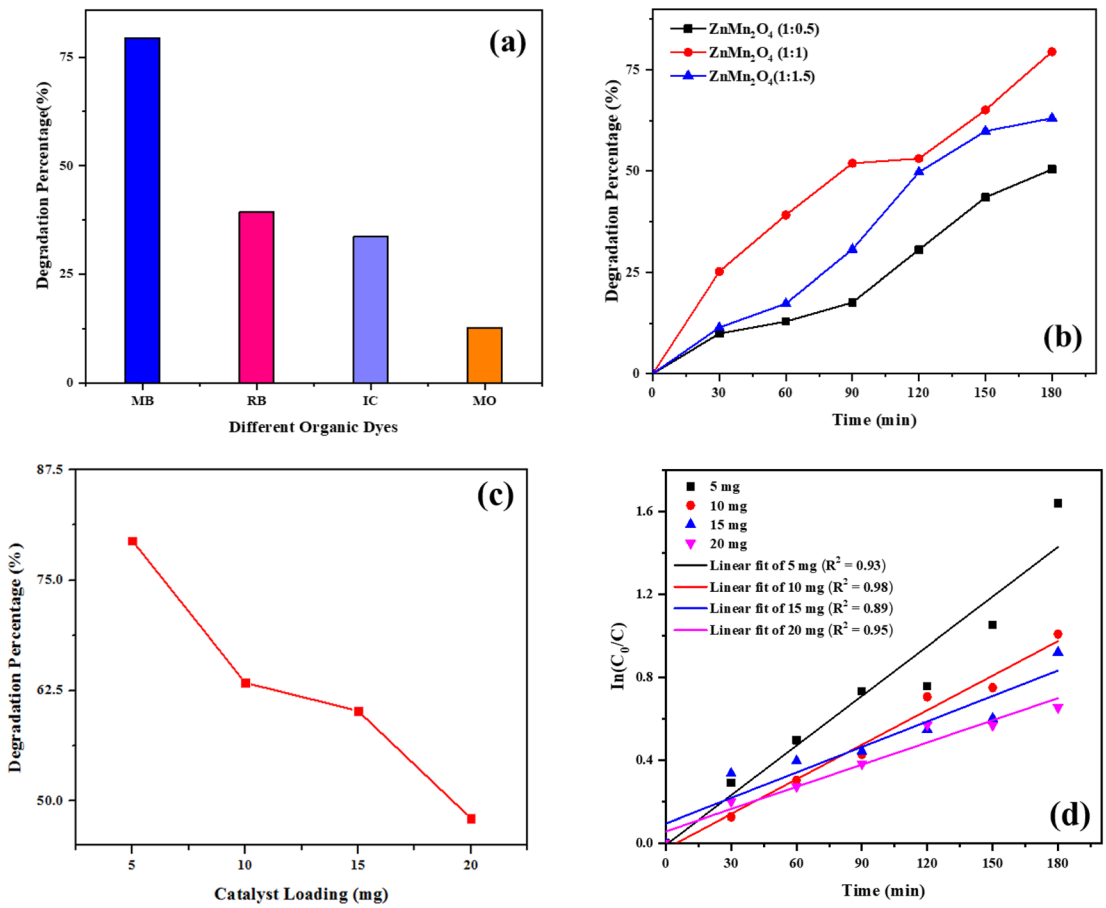

Fig. 8 (a) Photo-catalytic activity of $ZnMn_2O_4$NPs over different organic dyes (b) degradation percentage of MB in the presence of all $ZnMn_2O_4$ NPs; optimisation of catalytic dosage (5–20 mg) for degradation of MB dye in the presence of $ZnMn_2O_4$ (1 : 1) NPs at neutral pH (c) photocatalytic activity (d) rate constant.

Methylene Blue (MB), Rhodamine B (RB), Indigo Carmine (IC), and Methyl Orange (MO). A higher and good selectivity degradation of 79.45% ± 0.3% toward Methylene Blue (MB) dye was observed in the presence of $ZnMn_2O_4$ NPs with the *p*-value < 0.05, which proves it as statistically significant. The degradation was monitored by the alteration in the absorption spectra of the MB at λ_{max} at 665 nm. Thus, the reduction in the peak at 665 nm in the absorption spectra on exposure to UV light irradiation is attributed to the breakdown of the organic structure of MB. The capacity of the degradation was ascribed to its position of aromatic rings in the structure.[63] The degradation of MB dye in the presence of all synthesized $ZnMn_2O_4$ NPs is represented in Fig. 8b. $ZnMn_2O_4$ (1 : 1) NPs have shown the maximum degradation under UV light irradiation owing to their lower band gap than the other NPs, which helps more electrons to reach the conduction band, creating a huge number of holes in the valence band. These electrons and holes are responsible for the production of $^{\bullet}H$ and $O_2^{\bullet-}$radical, which acts as an active species and enhances the photo degradation of organic dyes.[64] Therefore, $ZnMn_2O_4$ (1 : 1) NPs show higher efficiency than the other synthesized NPs, and various factors influencing the photo degradation, such as catalytic load, dye concentration, and pH are optimized to increase the efficiency of the degradation of MB dye. Alongside photo stability of the NPs is also examined.

3.9.2. Optimization of photo degradation by various parameters

3.9.2.1. Catalytic dosage. To elevate the degradation efficiency of the MB dye solution (100 mL, 5 ppm), the catalyst dosage was optimized from 5–20 mg under UV light radiation at neutral pH. Fig. 8c illustrates the proportion of degradation of the MB dye solution gradually reduces with an increment in catalytic dosage. This can be attributed to the accumulation of more dye on the surface of the catalyst, causing the solution to be turbid and inhibiting its absorption of photons from the radiation.[65] This parameter of catalytic dosage implies that a minimum amount of catalytic load is required for the maximum efficiency of degradation of the MB dye solution. Therefore, the rest of the experiments were conducted in a 5 mg optimized catalytic amount.

3.9.2.2. Dye concentration. Dye concentration has a significant role in the photo degradation. To optimize the maximum efficiency of photo degradation of MB dye solution in the presence of $ZnMn_2O_4$ NPs (5 mg) was done by proliferating the dye concentration was proliferated from 5–20 ppm under UV light radiation at neutral pH. Fig. 9a represents the percentage

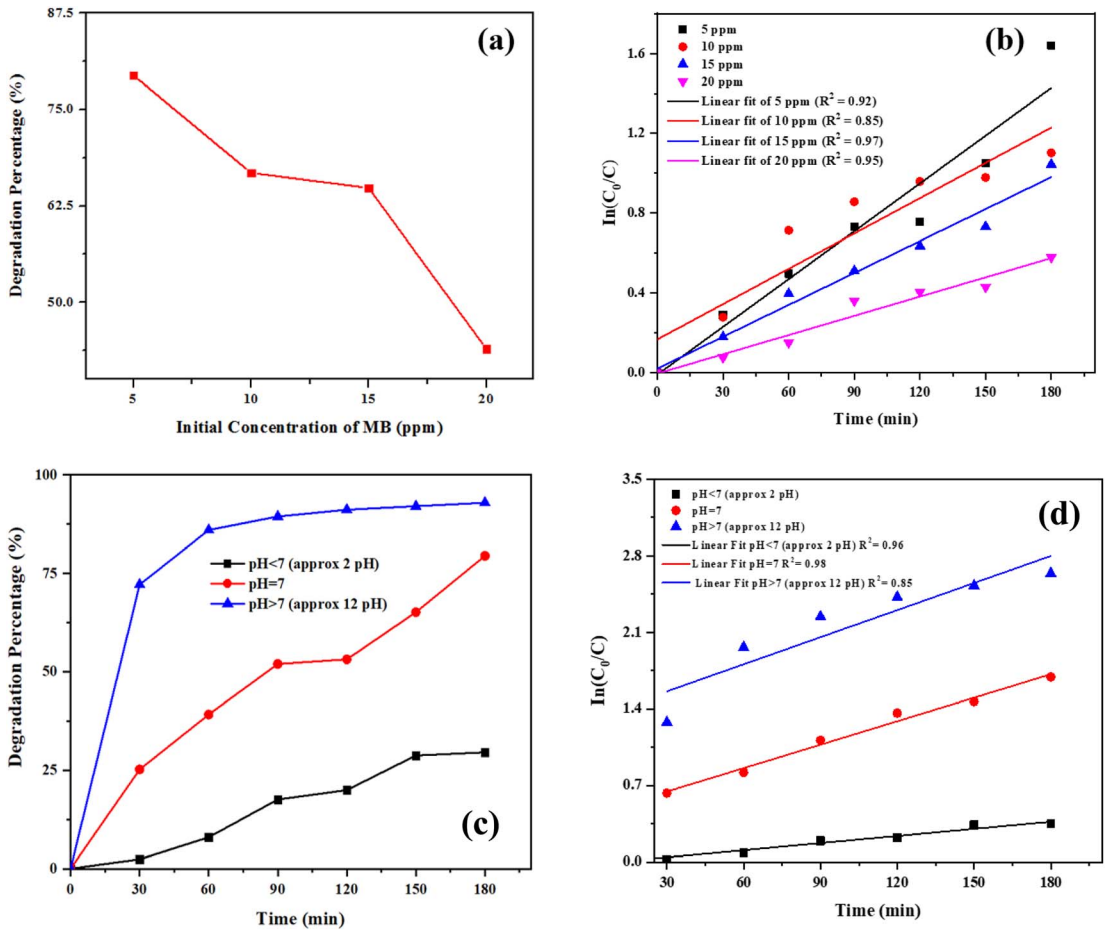

Fig. 9 Optimisation of dye concentration (5–20 ppm) for degradation of MB dye in the presence of $ZnMn_2O_4$ (1 : 1) NPs at neutral pH (a) photocatalytic activity (b) rate constant; optimisation of pH values for degradation of MB dye in the presence of $ZnMn_2O_4$ (1 : 1) NPs at neutral pH (c) photocatalytic activity (d) rate constant.

of degradation of the MB dye solution reduced on increasing the dye concentration from 5–20 ppm. This can be explained *via* Beer–Lambert law, which states that on increasing the concentration of the dye, the path length of photons absorbed by the NPs decreases and resulting in limited production of active radicals ($O_2^{\bullet -}$, $^{\bullet}H$).[66] Thus, this parameter indicates lower dye concentration is optimum for maximum degradation percentage. Hence, the optimum 5 ppm concentration of MB dye solution was utilized for further experiments.

3.9.2.3. pH variation. Optimizing the pH parameter is the most fundamental part of dye degradation. To evaluate this parameter, photodegradation of the MB dye solution was conducted at various pH levels with optimized catalytic dosage and dye concentration. The pH values were adjusted to acidic and basic using 0.1 N H_2SO_4 and 0.1 N NaOH. Fig. 9c demonstrated that degradation percentage reached a maximum efficiency of 92.86% ± 0.1% in basic medium, and acidic medium showed a reduction in the degradation percentage efficiency of 29.52% ± 0.5%. These changes can be ascribed to the surface charge of $ZnMn_2O_4$ NPs, which is negative, that adsorbs cationic dyes. As the pH values increase, the surface charge of the $ZnMn_2O_4$ NPs becomes more negative and the adsorption of MB dye increases, leading to higher efficiency of MB dye degradation.[51] Therefore, the degradation of the MB dye solution by $ZnMn_2O_4$ NPs is significantly higher in a basic medium.

3.9.3. Degradation kinetics. Kinetic analyses were carried out to determine the optimum conditions for the photocatalytic degradation of MB dye. Figure 8d, 9b, and 9d illustrate that photodegradation of dye follows pseudo-first-order kinetics, where the slope represents the rate constant (k) calculated from the $\ln(C_0/C)$ *versus* reaction time described by Langmuir and Hinshelwood model, defined as.

$$C = C_0 e^{-kt} \quad (17)$$

$$\ln(C_0/C) = kt \quad (18)$$

The k values for the corresponding catalytic loads, dye concentration, and pH are represented in Tables S3–S5, SI. Thus, the slope with higher k values is observed in 5 mg catalytic load, 5 ppm dye concentration, and in basic pH, which verifies the experimental results. Hence, photodegradation was conducted with the optimized parameters of 5 mg $ZnMn_2O_4$ NPs in 5 ppm MB dye concentration under UV light source at neutral pH, which is depicted in Fig. S4 and the data show consistent results with the literature, which is shown in Table 4.

3.9.4. Mechanism of photo degradation. To determine the mechanism of photo degradation of MB dye by $ZnMn_2O_4$, a radical trapping experiment was carried out in which scavengers such as Ascorbic acid (10 mM), $K_2Cr_2O_7$ (10 mM), EDTA (10 mM), and *tet*-butyl (1 : 20 v/v) alcohol was incorporated into different mixtures of MB dye solution for trapping $^{\bullet}H$, $O_2^{\bullet -}$, h^+ and e^-. It was observed that $K_2Cr_2O_7$ and butyl alcohol suppressed and dropped the percentage degradation of the MB dye solution to 55.89% ± 0.6% and 54.24% ± 0.3%, as shown in Fig. 11a. Thus, the scavenging properties of $K_2Cr_2O_7$ and *t*-butyl alcohol towards e^- and $^{\bullet}H$ radical revealed that these active species govern the overall photo degradation of MB dye by $ZnMn_2O_4$ NPs than the h^+ and $O_2^{\bullet -}$ radical.

As the $^{\bullet}H$ radical prevails to be the active species that governs the overall photodegradation process determination of $^{\bullet}H$ radicals becomes important. Therefore, a simple experiment of converting coumarin to 7-hydroxycoumarin by the $^{\bullet}H$ radicals released during photo oxidation of water, by taking 5 mg of $ZnMn_2O_4$ (1 : 1) NPs in 100 mL of 10 mM coumarin solution and irradiating under UV light.[42] At an interval of 10 min, the solution was collected and at excitation of 440 nm the fluorescence spectra were recorded. Fig. S5 divulged the increasing intensity on the increasing concentration of 7-hydroxycoumarin formed. This confirms that $ZnMn_2O_4$ generates $^{\bullet}H$ radicals on photo oxidation with water molecules.

The primary factors influencing the photo degradation of nanoparticles are their reduced band gap, surface area, and electron/hole separation efficiency. Fig. 10 provides a schematic illustration of the deterioration mechanism. $ZnMn_2O_4$ (1 : 1) NPs have a large surface area and a higher e^-/h^+ separation. As previously mentioned, h^+ and $^{\bullet}H$ radicals actively contribute to the photo degradation of MB dye. The e^- from the valence band migrates towards the conduction band upon irradiation by a UV light source, producing h^+. The generated h^+ and e^- oxidize and reduce H_2O respectively, which aid the production of $^{\bullet}H$ and $O_2^{\bullet -}$ radicals.[53] These radicals accumulate on the surface of NPs and help break down the organic structure of MB dye into CO_2 and H_2O.

3.9.5. Photostability and reusability. Regarding the application of nanoparticles in industry to degrade dyes, the reusability of the nanoparticles plays a crucial role. Thus, stability and reusability of $ZnMn_2O_4$ NPs were examined by removing the NPs from the MB dye solution through centrifugation, washed with distilled water and methanol, then dried in the oven for 3 h at 100 °C. Fig. 11b displays the percentage degradation of MB

Table 4 Literature survey for the photodegradation of methylene blue by NPs

S. no	Nanoparticles	Synthesis method	Degradation material	Degradation percentage	Reference
1	P25 TiO_2	Commerical	Methylene blue	81.4%	67
2	ZnO	Co-precipitation method	Methylene blue	66%	68
3	α-Fe_2O_3	Co-precipitation method	Methylene blue	78%	69
4	Bi doped TiO_2	Wet impregnation method	Methylene blue	80%	70
5	$MnTiO_3$	Sol–gel method	Methylene blue	70%	71
6	$ZnMn_2O_4$	Co-precipitation method	Methylene blue	77%	72
7	$ZnMn_2O_4$	Green combustion method	Methylene blue	79.45%	Present

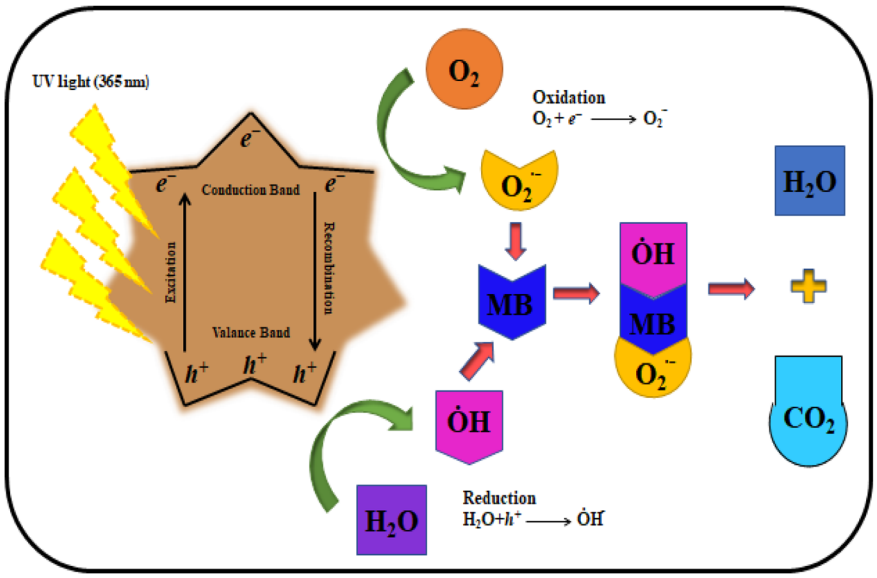

Fig. 10 Mechanism of photocatalytic degradation of $ZnMn_2O_4$ NPs.

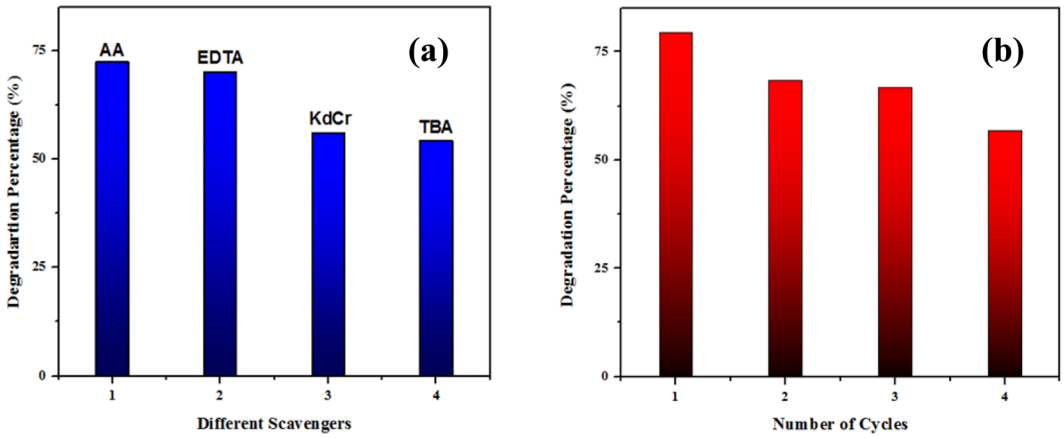

Fig. 11 (a) Effects of different scavengers during the degradation of MB dye (b) photostability and reusability of $ZnMn_2O_4$ (1 : 1) NPs over four successive cycles.

dye with the optimum concentration at neutral pH during the course of four cycles. It was observed that until 3rd cycle there was no significant change in the percentage degradation but 4th cycle shows reduction in degradation percentage of dye solution. Thus, stability of the $ZnMn_2O_4$ reduces after the 3rd cycle owing to devastation of the $ZnMn_2O_4$ structure, limiting the efficiency of dye degradation.

3.10. Detoxification of chromium(IV) ions

Photocatalytic reduction of Cr(IV) to Cr(III) ions in the presence of a UV light source is shown in Fig. 12. The detoxification of Cr(IV) ions in aqueous medium was performed by introducing 5 mg of $ZnMn_2O_4$ NPs into 1 mM of $K_2Cr_2O_7$ solution and irradiating with UV light at neutral pH. A decrease in the characteristic peak of Cr(IV) ions in the absorption spectra at 350 nm was observed in the above figure, indicating the

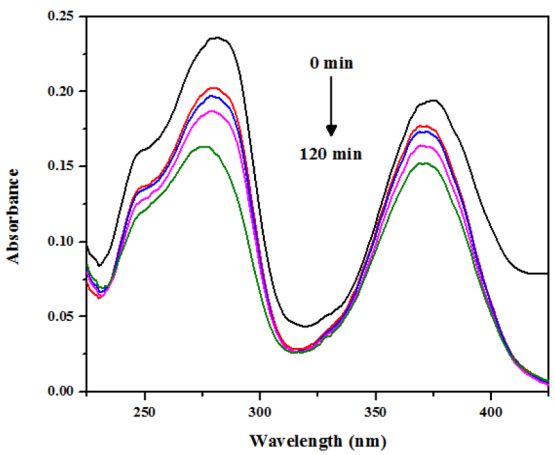

Fig. 12 Photocatalytic detoxification of Cr(IV) to Cr(III) ions in the presence of UV light source (365 nm).

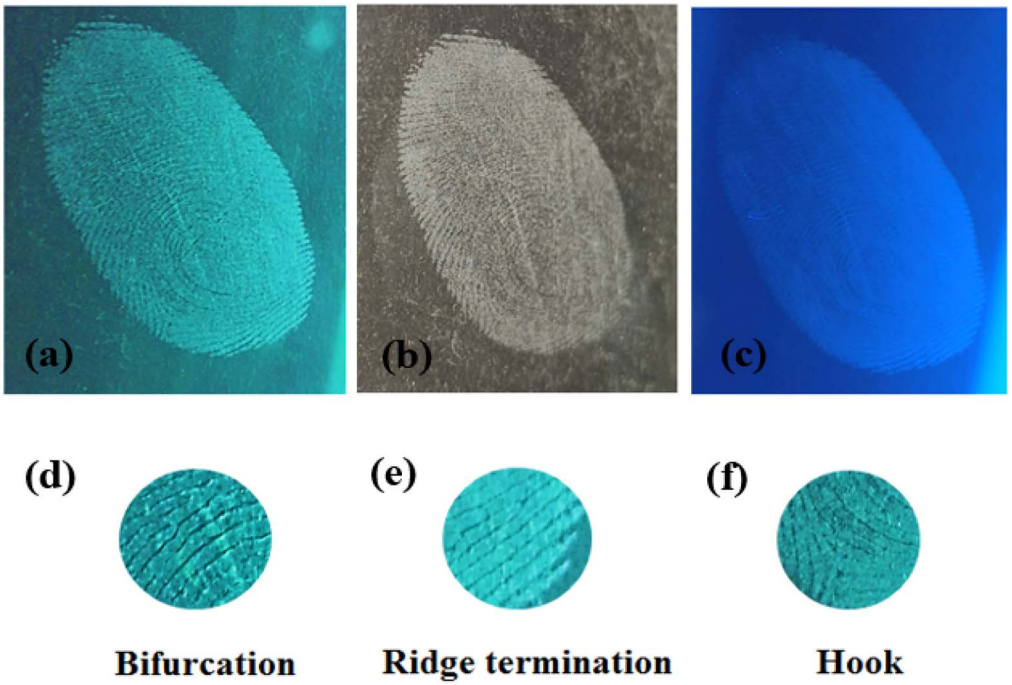

Fig. 13 LFPs displayed on mobile phone by $ZnMn_2O_4$ NPs (a) on exposure to UV light (254 nm) (b) on exposure to visible light (c) on exposure to UV light (365 nm), secondary level features (d) bifurcation (e) ridge termination (f) hook.

reduction of Cr(IV) to Cr(III) ions in aqueous medium. This decrement reached its saturation at 120 min, implying there is no further reduction of Cr(IV) to Cr(III) ions. This is due to the complete utilization of electrons generated by $ZnMn_2O_4$ NPs on irradiation with a UV light source, and no electrons are available to propagate the reduction process.

3.10.1. Mechanism of photoreduction of chromium(IV). The mechanism of photocatalytic reduction of Cr(IV) to Cr(III) ions in aqueous medium is represented schematically below. When $ZnMn_2O_4$ NPs are irradiated with UV light, electrons from the valence band move to the conduction band, generating holes/electrons (h^+/e^-) in the system. As the reduction of chromium(IV) takes place in acidic medium, the generated h^+ reacts with H_2O, producing H^+ and creating the optimum condition for the reduction to take place. The dichromate Cr(IV) ions in the aqueous medium takes up these electrons in the presence of H^+ ions and reduces itself to Cr(III) ions.[44] Hereby, detoxification of Cr(IV) ions in aqueous medium is achieved.

$$ZnMn_2O_4 + h\nu \rightarrow ZnMn2O_4\ (h^+ + e^-)$$

$$2H_2O + 4h^+ \rightarrow O_2 + 4H^+$$

$$H_2O + h^+ \rightarrow OH^- + H^+$$

$$Cr_2O_7^{2-} + 14H^+ + 6e^- \rightarrow 2Cr^{3+} + 7H_2O$$

3.11. Latent fingerprinting (LFPs) analysis

The fluorescence emissive nature of $ZnMn_2O_4$ NPs under short UV light (254 nm) has been utilised in imaging latent fingerprints (LFPs). Before fingerprint collection, washing hands and gently rubbing fingers on the nose or forehead before pressing them onto different substrates is mandatory. To investigate the practical applicability, we used various surfaces such as a glass bowl, a mobile phone screen, and a CD drive for imaging purpose represented in Fig. S6. Dusting of the NPs on the fingerprints using a brush and displayed a bluish-green fluorescence on exposure to the Short UV light of 254 nm. The adhesive nature of NPs gets attached to sebum and sweat present in LFPs, exhibiting fluorescent ridges and non-fluorescent furrows for easy naked eye detection. The entire image presented in Fig. 13 is captured using ordinary mobile phone. Secondary level information including bifurcation, ridge termination and hook of LFPs are also captured clearly. The above result concludes $ZnMn_2O_4$ NPs can be used as tool for identification of fingerprint and solving crime cases.

4. Conclusion

In conclusion, bimetallic $ZnMn_2O_4$ NPs have been synthesized *via* the green combustion method using *Arachis hypogaea* seed powder as fuel. Various characterisation techniques such as XRD, FTIR, SEM, BET, UV-Vis, and PL spectroscopy have been employed to examine the structural, morphological, and optical properties of $ZnMn_2O_4$ NPs. The evaluation of the optical properties of the $ZnMn_2O_4$ NPs divulged a low band gap and cyan blue fluorescence nature of the NPs. Therefore, the synthesized $ZnMn_2O_4$ NPs were incorporated in multidisciplinary fields for the deterioration of industrial pollutants and latent fingerprinting applications. It showed an enhanced identification of secondary-level information in LFPs and efficient adsorption and photodegradation of methylene blue dye

under a UV light source. On the other hand, synthesized $ZnMn_2O_4$ NPs helped in the reduction of hexavalent chromium ions in aqueous medium owing to their production of a greater number of e^- during photoreduction. Thus, synthesized bimetallic $ZnMn_2O_4$ NPs can be seen as a multifaceted tool that can be used in multidisciplinary fields.

Conflicts of interest

The authors declare that there are no conflicts of interest.

Data availability

The authors confirm that the data supporting the findings of this study are available within the article and its SI. See DOI: https://doi.org/10.1039/d5ra05696a.

Acknowledgements

I would like to thank CHRIST (Deemed to be University), Bangalore, and Energy Materials Research Laboratory, Siddaganga Institute of Technology, Tumakuru for constant support and encouragement for research.

References

1 Z. H. Mohammad, F. Ahmad, S. A. Ibrahim and S. Zaidi, *Discover Food*, 2022, **2**, 12, DOI: 10.1007/s44187-022-00013-9.
2 S. Khaturia, M. Chahar, H. Sachdeva, Sangeeta and C. B. Mahto, *J. Nanomed. Nanotechnol.*, 2020, **11**(2), 1–16, DOI: 10.35248/2157-7439.19.10.543.
3 L. Wang, C. Hu and L. Shao, *Int. J. Nanomed.*, 2017, **12**, 1227–1249, DOI: 10.2147/IJN.S121956.
4 X. Huang, Y. Zhu and E. Kianfar, *J. Mater. Res. Technol.*, 2021, **12**, 1649–1672, DOI: 10.1016/j.jmrt.2021.03.048.
5 A. Hasan, M. Morshed, A. Memic, S. Hassan, T. J. Webster and H. E. S. Marei, *Int. J. Nanomed.*, 2018, **13**, 5637–5655, DOI: 10.2147/IJN.S153758.
6 I. Khan, K. Saeed and I. Khan, *Arab. J. Chem.*, 2019, **12**(7), 908–931, DOI: 10.1016/j.arabjc.2017.05.011.
7 L. Zhang, F. X. Gu, J. M. Chan, A. Z. Wang, R. S. Langer and O. C. Farokhzad, *Clin. Pharmacol. Therapeut.*, 2008, **83**(5), 761–769, DOI: 10.1038/sj.clpt.6100400.
8 R. A. Petros and J. M. DeSimone, *Nat. Rev. Drug Discov.*, 2010, **9**(8), 615–627, DOI: 10.1038/nrd2591.
9 M. Krystek and M. Górski, *New Uses Micro Nanomater.*, 2018, **8**, 201, DOI: 10.5772/intechopen.79995.
10 L. R. Yadav, S. Pratibha, K. Manjunath, M. Shivanna, T. Ramakrishnappa, N. Dhananjaya and G. Nagaraju, *J. Sci. Adv. Mater. Devices*, 2019, **4**(3), 425–431, DOI: 10.1016/j.jsamd.2019.03.001.
11 F. A. Alharthi, M. A. Alsaiari, M. S. Jalalah, M. Shashank, A. A. Alghamdi, J. S. Algethami and N. Ganganagappa, *Ceram. Int.*, 2021, **47**(7), 10291–10300, DOI: 10.1016/j.ceramint.2020.07.142.
12 M. Fondell, T. J. Jacobsson, M. Boman and T. Edvinsson, *J. Mater. Chem. A*, 2014, **2**(10), 3352–3363, DOI: 10.1039/c3ta14846g.
13 N. A. Albadarin, M. S. Takriff, S. T. Tan, S. A. Shahahmadi, L. J. Minggu, A. A. H. Kadhum, W. W. Yin, M. N. I. Salehmin, E. M. Alkhalqi, M. A. A. Hamid and N. Amin, *Mater. Res. Express*, 2020, **7**(12), 8, DOI: 10.1088/2053-1591/abd1e6.
14 Q. Ni, H. Cheng, J. Ma, Y. Kong and S. Komarneni, *Front. Chem. Sci. Eng.*, 2020, **14**(6), 956–966, DOI: 10.1007/s11705-019-1907-z.
15 E. Moyen, J. H. Kim, J. Kim and J. Jang, *ACS Appl. Nano Mater.*, 2020, **3**(6), 5203–5211, DOI: 10.1021/acsanm.0c00639.
16 B. Ludi and M. Niederberger, *Dalton Trans.*, 2013, **42**(35), 12554–12568, DOI: 10.1039/c3dt50610j.
17 Y. Sun, L. Chen, Y. Bao, Y. Zhang, J. Wang, M. Fu, J. Wu and D. Ye, *Catalysts*, 2016, **6**, 12, DOI: 10.3390/catal6120188.
18 S. Liu, C. Li, J. Yu and Q. Xiang, *CrystEngComm*, 2011, **13**(7), 2533–2541, DOI: 10.1039/c0ce00295j.
19 L. Duan, B. Sun, M. Wei, S. Luo, F. Pan, A. Xu and X. Li, *J. Hazard. Mater.*, 2015, **285**, 356–365, DOI: 10.1016/j.jhazmat.2014.12.015.
20 F. Cheng, J. Shen, B. Peng, Y. Pan, Z. Tao and J. Chen, *Nat. Chem.*, 2010, **3**(1), 79–84, DOI: 10.1038/nchem.931.
21 S. H. Khabbaz, A. Bagheri and M. Mousavi-Kamazani, *Heliyon*, 2025, **11**, e41294, DOI: 10.1016/j.heliyon.2024.e41294.
22 S. Zinatloo-Ajabshir, M. S. Morassaei and M. Salavati-Niasari, *Composites, Part B*, 2019, **167**, 643–653, DOI: 10.1016/j.compositesb.2019.03.045.
23 A. Sobhani, *Arab. J. Chem.*, 2023, **16**(10), 105201, DOI: 10.1016/j.arabjc.2023.105201.
24 A. Sobhani, *Int. J. Hydrogen Energy*, 2022, **47**(46), 20138–20152, DOI: 10.1016/j.ijhydene.2022.04.149.
25 A. Sobhani and S. Alinavaz, *Heliyon*, 2023, **9**, 11, DOI: 10.1016/j.heliyon.2023.e21979.
26 M. Wang, M. Li, A. Yu, Y. Zhu, M. Yang and C. Mao, *Adv. Funct. Mater.*, 2017, **27**, 14–1606243, DOI: 10.1002/adfm.201606243.
27 J. Xu, H. Yang, W. Fu, K. Du, Y. Sui, J. Chen, Y. Zeng, M. Li and G. Zou, *J. Magn. Magn Mater.*, 2007, **309**(2), 307–311, DOI: 10.1016/j.jmmm.2006.07.037.
28 A. N. P. Madathil, K. A. Vanaja and M. K. Jayaraj, In *Nanophotonic Materials IV*, 2007, 6639, 47–55, doi: DOI: 10.1117/12.730364.
29 R. Singaravelan and S. Bangaru Sudarsan Alwar, *Appl. Nanosci.*, 2015, **5**, 983–991, DOI: 10.1007/s13204-014-0396-0.
30 S. S. Patil, M. G. Mali, M. S. Tamboli, D. R. Patil, M. V. Kulkarni, H. Yoon, H. Kim, S. S. Al-Deyab, S. S. Yoon, S. S. Kolekar and B. B. Kale, *Catal. Today*, 2016, **260**, 126–134, DOI: 10.1016/j.cattod.2015.06.004.
31 B. Fardsadegh and H. Jafarizadeh-Malmiri, *Green Process. Synth.*, 2019, **8**(1), 399–407, DOI: 10.1515/gps-2019-0007.
32 Y. Wang, X. Sun, T. Xian, G. Liu and H. Yang, *Opt. Mater.*, 2021, **113**, 110853, DOI: 10.1016/j.optmat.2021.110853.

33 Y. Park, G. A. Ayoko and R. L. Frost, *J. Colloid Interface Sci.*, 2011, **354**(1), 292–305, DOI: 10.1016/j.jcis.2010.09.068.
34 K. S. Rajmohan, R. Chandrasekaran and S. Varjani, *Indian J. Microbiol.*, 2020, **60**(2), 125–138, DOI: 10.1007/s12088-019-00841-x.
35 R. Kishor, D. Purchase, G. D. Saratale, R. G. Saratale, L. F. R. Ferreira, M. Bilal, R. Chandra and R. N. Bharagava, *J. Environ. Chem. Eng.*, 2021, **9**(2), 105012, DOI: 10.1016/j.jece.2020.105012.
36 S. Wong, N. A. Ghafar, N. Ngadi, F. A. Razmi, I. M. Inuwa, R. Mat and N. A. S. Amin, *Sci. Rep.*, 2020, **10**, 2928, DOI: 10.1038/s41598-020-60021-6.
37 M. R. Gadekar and M. M. Ahammed, *Desalination Water Treat.*, 2016, **57**(55), 26392–26400, DOI: 10.1080/19443994.2016.1165150.
38 G. Rajhans, A. Barik, S. K. Sen and S. Raut, *Biotechnologia*, 2021, **102**(4), 445, DOI: 10.5114/bta.2021.111109.
39 R. Javaid and U. Y. Qazi, *Int. Res. J. Publ. Environ. Health*, 2019, **16**, 11–2066, DOI: 10.3390/ijerph16112066.
40 K. Sirirerkratana, P. Kemacheevakul and S. Chuangchote, *J. Clean. Prod.*, 2019, **215**, 123–130, DOI: 10.1016/j.jclepro.2019.01.037.
41 A. Rafiq, M. Ikram, S. Ali, F. Niaz, M. Khan, Q. Khan and M. Maqbool, *J. Ind. Eng. Chem.*, 2021, **97**, 111–128, DOI: 10.1016/j.jiec.2021.02.017.
42 S. B. Patil, H. S. Bhojya Naik, G. Nagaraju and Y. Shiralgi, *Eur. Phys. J. Plus*, 2018, **133**(6), 229, DOI: 10.1140/epjp/i2018-12063-5.
43 A. Shahzaib, N. Nishat, S. M. Alshehri, T. Ahamad and Z. Haque, *Hybrid Adv.*, 2024, **5**, 100145, DOI: 10.1016/j.hybadv.2024.100145.
44 T. N. Ravishankar, S. Muralikrishna, G. Nagaraju and T. Ramakrishnappa, *Anal. Methods*, 2015, **7**, 3493–3499, DOI: 10.1039/C5AY00096C.
45 M. Khammar, F. Ynineb, S. Guitouni, Y. Bouznit and N. Attaf, *Appl. Phys. A*, 2020, **126**(6), 398, DOI: 10.1007/s00339-020-03591-6.
46 T. Abdel-Baset, S. Saber and S. El-Sayed, *J. Mater. Sci.: Mater. Electron.*, 2020, **31**(23), 20972–20983, DOI: 10.1007/s10854-020-04611-0.
47 V. PS and K. VT, *Int. J. Environ. Anal. Chem.*, 2022, **104**(17), 5038–5098, DOI: 10.1080/03067319.2022.2118581.
48 M. Ramesh, M. Anbuvannan and G. Viruthagiri, *Spectrochim. Acta, Part A*, 2015, **136**, 864–870, DOI: 10.1016/j.saa.2014.09.105.
49 Udayabhanu, G. Nagaraju, H. Nagabhushana, R. B. Basavaraj, G. K. Raghu, D. Suresh, H. Rajanaika and S. C. Sharma, *Cryst. Growth Des.*, 2016, **16**(12), 6828–6840, DOI: 10.1021/acs.cgd.6b00936.
50 A. Ummadisingu, S. Meloni, A. Mattoni, W. Tress and M. Grätzel, *Angew. Chem., Int. Ed.*, 2021, **60**(39), 21368–21376, DOI: 10.1002/anie.202106394.
51 S. Chaturvedi, R. Das, P. Poddar and S. Kulkarni, *RSC Adv.*, 2015, **5**(30), 23563–23568, DOI: 10.1039/c5ra00933b.
52 S. Kumar, S. Pal, J. Kuntail and I. Sinha, *Environ. Nanotechnol. Monit. Manag.*, 2019, **12**, 100236, DOI: 10.1016/j.enmm.2019.100236.
53 H. Ullah, L. Mushtaq, Z. Ullah, A. Fazal and A. M. Khan, *Inorg. Nano-Met. Chem.*, 2021, **51**(7), 963–975, DOI: 10.1080/24701556.2020.1813766.
54 M. Mousavi, A. Habibi-Yangjeh and M. Abitorabi, *J. Colloid Interface Sci.*, 2016, **480**, 218–231, DOI: 10.1016/j.jcis.2016.07.021.
55 T. L. Soundarya, R. Harini, K. Manjunath, B. Nirmala and G. Nagaraju, *Int. J. Hydrogen Energy*, 2023, **48**(82), 31855–31874, DOI: 10.1016/j.ijhydene.2023.04.289.
56 Z. R. Khan, M. Shkir, V. Ganesh, I. S. Yahia and S. AlFaify, *Indian J. Phys.*, 2021, **95**, 43–49, DOI: 10.1007/s12648-020-01695-6.
57 C. Shamitha, T. Senthil, L. Wu, B. S. Kumar and S. Anandhan, *J. Mater. Sci.: Mater. Electron.*, 2017, **28**, 15846–15860, DOI: 10.1007/s10854-017-7479-0.
58 P. Koohi, A. Rahbar-Kelishami and H. Shayesteh, *Environ. Technol. Innovat.*, 2021, **23**, 101559, DOI: 10.1016/j.eti.2021.101559.
59 G. Jethave, U. Fegade, S. Attarde, S. Ingle, M. Ghaedi and M. M. Sabzehmeidani, *Heliyon*, 2019, **5**, e02412, DOI: 10.1016/j.heliyon.2019.e02412.
60 S. Y. Lagergren, Kungliga Svenska Vetenskapsakad, *Handlingar*, 1898, **24**, 1–39.
61 Y. Ho and G. McKay, *Process Biochem.*, 1999, **34**(5), 451–465, DOI: 10.1016/S0032-9592(98)00112-5.
62 A. Saha, B. B. Basak and M. Ponnuchamy, *Sep. Sci. Technol.*, 2020, **55**(11), 1970–1983, DOI: 10.1080/01496395.2019.1620277.
63 K. C. Chen, J. Y. Wu, D. J. Liou and S. C. J. Hwang, *J. Biotechnol.*, 2003, **101**(1), 57–68, DOI: 10.1016/S0168-1656(02)00303-6.
64 G. Nagaraju, S. A. Prashanth, M. Shastri, K. V. Yathish, C. Anupama and D. Rangappa, *Mater. Res. Bull.*, 2017, **94**, 54–63, DOI: 10.1016/j.materresbull.2017.05.043.
65 R. Sharma, S. Bansal and S. Singhal, *RSC Adv.*, 2015, **5**(8), 6006–6018, DOI: 10.1039/c4ra13692f.
66 M. H. Habibi, N. Talebian and J. H. Choi, *Dyes Pigments*, 2007, **73**(1), 103–110, DOI: 10.1016/j.dyepig.2005.10.016.
67 S. M. Tichapondwa, J. P. Newman and O. Kubheka, *Phys. Chem. Earth, Parts A/B/C*, 2020, **118**, 102900, DOI: 10.1016/j.pce.2020.102900.
68 A. Negash, S. Mohammed, H. D. Weldekirstos, A. D. Ambaye and M. Gashu, *Sci. Rep.*, 2023, **13**(1), 22234, DOI: 10.1038/s41598-023-48826-7.
69 M. B. Goudjil, H. Dali, S. Zighmi, Z. Mahcene and S. E. Bencheikh, *Desalination Water Treat.*, 2024, **317**, 100079, DOI: 10.1016/j.dwt.2024.100079.
70 S. Mishra, N. Chakinala, A. G. Chakinala and P. K. Surolia, *Catal. Commun.*, 2022, **171**, 106518, DOI: 10.1016/j.catcom.2022.106518.
71 S. Alkaykh, A. Mbarek and E. E. Ali-Shattle, *Heliyon*, 2020, 6–4, DOI: 10.1016/j.heliyon.2020.e03663.
72 K. F. Fawy, M. F. Ashiq, F. F. Alharbi, S. Manzoor, M. U. Nisa, M. Ibrahim, M. T. N. Khan, M. Messali, A. H. Chughtai and M. N. Ashiq, *J. Taibah Univ. Sci.*, 2024, **18**(1), 2302656, DOI: 10.1080/16583655.2024.2302656.